1   **Substrate ligand density modulates gap junction intercellular communication**

2   **during mesenchymal cell condensation**

3   Ignasi Casanellas[a,b,c], Anna Lagunas[c,a]*, Yolanda Vida[d,e], Ezequiel Pérez-Inestrosa[d,e], Cristina Rodríguez-

4   Pereira[f], Joana Magalhaes[c,f], José A. Andrades[g,c,e], José Becerra[g,c,e], Josep Samitier[a,b,c]

5

6   [a]Institute for Bioengineering of Catalonia (IBEC), Barcelona Institute of Science and Technology (BIST). c/ Baldiri

7   Reixac, 10-12, 08028 Barcelona, Spain.

8   [b]Department of Electronics and Biomedical Engineering, University of Barcelona (UB), Faculty of Physics. c/ Martí

9   i Franquès, 1, 08028 Barcelona, Spain.

10   [c]Biomedical Research Networking Center in Bioengineering, Biomaterials, and Nanomedicine (CIBER-BBN). Av.

11   Monforte de Lemos, 3-5. Pabellón 11. Planta 0, 28029 Madrid, Spain.

12   [d]Universidad de Málaga - IBIMA, Dpto. Química Orgánica. Campus de Teatinos s/n, 29071 Málaga, Spain.

13   [e]Centro Andaluz de Nanomedicina y Biotecnología-BIONAND. Parque Tecnológico de Andalucía, c/ Severo Ochoa

14   35, 29590 Campanillas, Málaga, Spain.

15   [f]Unidad de Medicina Regenerativa, Grupo de Investigación en Reumatología (GIR), Instituto de Investigación

16   Biomédica de A Coruña (INIBIC), Complexo Hospitalario Universitario de A Coruña (CHUAC), Sergas,

17   Universidade da Coruña (UDC). c/ Xubias de Arriba, 84, 15006 A Coruña, Spain.

18   [g]Department of Cell Biology, Genetics and Physiology, Universidad de Málaga (UMA), Instituto de Investigación

19   Biomédica de Málaga (IBIMA). Av. Cervantes, 2, 29071 Málaga, Spain.

20   *Corresponding author: alagunas@ibecbarcelona.eu

21

22   **Abstract**

23   Gap junction intercellular communication (GJIC) provides a continuous and efficient flow of biological

24   information during tissue formation and is essential to sustain homeostasis and function in living

25   organisms. Cell-matrix interactions have been widely addressed and their influence on tissue organization

26   is recognized. However, how extracellular matrix (ECM) adhesion affects intercellular communication

27   during tissue formation remains elusive. Here we use substrates with uneven nanopatterns of adhesive

28   ligand arginine-glycine-aspartic acid (RGD) to control cell adhesion during mesenchymal condensation, a

29   prevalent morphogenetic transition. We show that the establishment of GJIC is an adhesion-gated

30   mechanism, which is dynamically regulated. Substrate effects continuously propagate into the forming

31   tissue through actomyosin contraction, affecting both the 3D architecture and functionality of the GJIC

32   network developing in prechondrogenic condensates.

33

34   *Keywords:* Dendrimer-based nanopatterning, arginine-glycine-aspartic acid (RGD), cell adhesion,

35   mesenchymal stem cells (MSCs), condensation, gap junction intercellular communication (GJIC).

1. Introduction

Mesenchymal cell condensation is a prevalent morphogenetic transition regulated by cell adhesion in which mesenchymal stem cells (MSCs) gather to form intimate cell-to-cell contacts [1]. The condensation phase was named "membranous skeleton" by Grüneberg to stress its distinctive function in skeletal development [2]. During skeletogenesis, cell density increases locally at the condensation sites by means of extracellular matrix (ECM)-driven active cell movement,[1] with an important role of the ECM ubiquitous protein fibronectin (FN), which is upregulated during mesenchymal condensation [3,4]. Cell condensates progressively evolve into cartilaginous nodules, setting the bases for cartilage formation.

In osteochondral development, mesenchymal cell condensation is concurrent with the formation of an extensive gap junction (GJ) communication network [5]. GJs are plasma membrane channels that provide intercellular and cell-matrix communication in almost all animal tissues, allowing cells to exchange ions and small molecules through a controlled gating mechanism [6]. During morphogenesis, an efficient network of GJs is an extremely versatile communication system that mediates the rapid synchronization between cells. GJs established during embryonic patterning allow multicellular groups to coordinate towards the formation of supracellular, tissue-level structures. Avascular tissues, such as cartilage, particularly rely on this form of intercellular communication for successful development [7–9].

Although previous studies have related gap junction intercellular communication (GJIC) with matrix-associated proteins [10–13], little is known about how extracellular inputs modulate the formation of intercellular GJ networks and the associated implications in tissue architecture and function. Integrin-mediated cell-matrix interactions have been shown to regulate many biological processes such as cell shape, proliferation, migration, differentiation and programmed cell death [14–16]. During morphogenesis, dynamic adhesion mechanisms, together with the associated regulatory signalling pathways, define tissue differentiation and architecture, and modulate collective cell behaviour [17–19].

Cell adhesion is governed at the nanoscale, as evidenced by the assembly of collagen fibres in the ECM or the folding/unfolding of fibronectin [20–22], and also by the compartmentalization of the cell membrane receptors into nanoclusters, which facilitates the allosteric regulation, increases the ligand rebinding probability and triggers the assembly of signalling complexes in the cytosol [23]. The nanopatterning of ECM motifs for the study of cell-surface interactions at the nanoscale highlighted the relevance of ECM ligand presentation to cells. Experiments using micellar lithography to create nanopatterns of the cell adhesive peptide arginine-glycine-aspartic acid (RGD) of fibronectin (FN), unveiled a nanospacing threshold of around 70 nm for an efficient cell adhesion on stiff substrates, and demonstrated that cell adhesion is more affected by the local rather than the global ligand concentrations

69   [24–27]. Since these first works in the field, others have emerged showing that not only cell adhesion, but

70   also many other cell responses are affected by the nanoscale ligand presentation [28].

71   In previous works, we have shown that a dendrimer-based RGD nanopatterning technique produces

72   uneven nanopatterns of tuneable local surface adhesiveness with liquid-like order and defined spacing on

73   large areas, thus being fully compatible with standard cell culture protocols [29]. Owing to steric

74   hindrance restrictions, each dendrimer of 4-5 nm in diameter, although bearing up to eight copies of the

75   RGD ligand, provides a single site for integrin receptor binding. Therefore, dendrimer nanopattern

76   configuration directly correlates with the RGD available for cell adhesion. The local surface adhesiveness

77   in the nanopatterns is obtained by quantifying the percentage of surface area with a minimum interparticle

78   distance below the 70 nm threshold for an efficient cell adhesion. These nanopatterns proved to sustain

79   cell adhesion more efficiently than the corresponding homogeneous surfaces [29] and improve cell

80   differentiation [30–32].

81   Taking chondrogenesis as a model [33], we used the RGD dendrimer-based nanopatterns to conduct a

82   systematic study of the influence of local surface adhesiveness on the establishment of GJIC network

83   during mesenchymal 3D condensation. Results show that local surface adhesiveness triggers cell

84   condensate responses from a threshold nanopattern configuration and we demonstrate that the adhesive

85   substrate information, which is transduced by integrins, propagates within cell condensates in a

86   continuous feedback mode through cytoskeletal contractility.

87

88   **2.   Methods**

89

90   *2.1. Production of nanopatterned substrates*

91

92   All steps were performed in a sterile tissue culture hood, and only sterile materials, solutions and

93   techniques were used. All dendrimer solutions were sonicated and filtered through a Millex RB sterile

94   syringe filter (Merk Millipore) prior to use, and stock solutions were used within 6 months of preparation.

95   Nanopatterned substrates were prepared as previously described [30,31]. Briefly, a 95/5 L-lactide/DL-

96   lactide copolymer (Corbion) 2% m v^{-1} solution in dry 1,4-dioxane (Sigma-Aldrich, 296309) was spin-

97   coated at 3000 rpm for 30 s on 1.25×1.25 cm Corning® glass microslides (Sigma-Aldrich). Deionized

98   water (18 MΩ·cm Milli-Q, Millipore) was used for rinsing samples and to prepare RGD-functionalized

99   dendrimers' working solutions at 2.5 10^{-8}, 10^{-8} and 4 10^{-9}% w w^{-1} concentrations. Spin-coated on poly(L-

100 lactic acid) (PLLA) substrates were treated for 13 min under UV light and immersed in dendrimer

101 solutions for 16 h (pH = 5.6, T = 293 K). Then, the nanopatterned substrates were rinsed with copious

3

102   amounts of water and dried. Positive controls (S_{FN}) were obtained by incubating spin-coated PLLA

103   substrates with fibronectin (100 μg mL^{-1}) from bovine plasma-solution (Sigma-Aldrich, F1141).

104   Nanopatterned substrates were imaged by atomic force microscopy (AFM) in a Dimension 3100 AFM

105   instrument (Veeco Instruments) operated in tapping mode at room temperature in air. Silicon AFM probes

106   (Budget Sensors) with a spring constant k = 40 N m^{-1} and a resonant frequency ν = 300 kHz were used. At

107   least three images of 5x5 μm were taken per substrate of three independent substrates per condition

108   (initial dendrimer concentration in solution). The AFM height images were processed with WSxM 4.0

109   software [34]. Corresponding image thresholds were obtained manually and processed with ImageJ

110   software (NIH). The resulting particle positions were used to obtain the minimum interparticle distances

111   (d_{min}) using a custom-generated MATLAB code (The MATHWORKS, Inc.), and the corresponding

112   probability contour plots for d_{min} were constructed using an adapted MATLAB code [29]. At least three

113   images from independent samples were computed. Quantification of the percentage of the area with a d_{min}

114   threshold below 70 nm in the d_{min} probability contour plots was performed by manually selecting the

115   regions and processing them with ImageJ.

116

117   *2.2. Cell culture*

118

119   Human adipose-derived MSCs (ATCC, PCS-500-011) were cultured at 37˚C and 5% CO_2 in MSC Basal

120   Medium (ATCC, PCS-500-030) supplemented with MSC Growth Kit Low Serum (ATCC, PCS-500-

121   040). Medium was replaced every 2 days. Passaging was carried out when cells reached 70-80%

122   confluence. For the experiments, cells were trypsinized at passages 3 to 4, counted, resuspended in

123   chondrogenesis-inducing medium Chondrocyte Differentiation Tool (ATCC, PCS-500-051) with 0.1% v

124   v^{-1} penicillin-streptomycin (Invitrogen, 15140), and seeded on nanopatterned and control substrates at a

125   density of 2,760 cells cm^{-2}. 3 replicates of each condition were seeded. Medium was replaced every 3

126   days.

127

128   *2.3. Immunostaining*

129

130   After 6 and 9 days of chondrogenic differentiation on the nanopatterns and controls, cells were carefully

131   rinsed with PBS (Gibco, 21600-10), fixed with Formalin Solution (Sigma, HT5011) for 20 min at room

132   temperature, and rinsed again twice with PBS. Aldehyde groups were blocked with 50 mM ammonium

133   chloride (Sigma, A9434) in PBS for 20 min. Samples were permeabilized with saponin (Sigma, 47036)

134   0.1% m v^{-1} in BSA (Sigma, A3059) 1% m/v in PBS for 10 min.

4

135   For connexin 43 (Cx43) and cell nuclei observation in cell condensates, samples were stained with rabbit

136   anti-Cx43 (Abcam, ab63851) antibody at 5 µg mL^{-1} in BSA 1% m v^{-1} in PBS for 1 h at room temperature,

137   then with anti-rabbit Alexa 568 (LifeTech, A11036) and Hoechst (Invitrogen, H3570) 1 µg mL^{-1} in BSA

138   1% m v-1 in PBS for 1 h. Samples were prepared with coverslips in Fluoromount mounting medium

139   (Sigma, HT5011).

140

141   *2.4. Image acquisition and analysis*

142

143   Samples were imaged with a Leica SPE Upright Confocal Microscope (Leica Microsystems) with a

144   40x/1.15 NA objective. The distance between imaged slices (z-size) was set at 1 µm. At least 3 cell

145   condensates were imaged for each sample.

146   Images were analyzed with ImageJ software. For condensate size measurements, a z-projection of each

147   condensate was created, and the whole condensate area was manually selected and measured. For the

148   measurement of Cx43 expression confocal z-projections were used (maximum stained area per sample).

149   Briefly, the background of z-projections was removed, and a threshold was applied to select areas of

150   Cx43 expression. The obtained total area was normalized against the area of the corresponding

151   condensate.

152   For the analysis of GJIC network, a threshold was applied to the Cx43 confocal stack and then it was

153   skeletonized with the ImageJ plugin (Fig. S1, Video S1). The resulting Cx43 network was analyzed to

154   retrieve the number of end-point voxels and the mean branch length in each condensate, which were

155   normalized to the Cx43 expression area and the number of slices taken for analysis. GJIC was calculated

156   as the inverse value of the end-point voxels.

157

158   *2.5. RNA extraction and retrotranscription*

159

160   Reverse transcription real-time PCR (RT-qPCR) was performed to measure Cx43 (*GJA1*) expression.

161   After 6 and 9 days of differentiation, mRNA was extracted from the samples and purified with a RNeasy

162   Micro Kit (Qiagen, 74004). Extracted mRNA was quantified in a Nanodrop ND-1000 Spectrophotometer

163   (Thermo Fisher Scientific). Reverse transcription for cDNA production was performed with an iScript

164   Advanced cDNA Synthesis Kit (Bio-Rad, 1725037) in a T100 Thermal Cycler (Bio-Rad). Three cell

165   culture replicates of each condition were obtained, with their RNA extracted and retrotranscribed. The

166   same procedure was performed on undifferentiated human mesenchymal stem cells (hMSCs) as a

167   reference.

168

169 *2.6. qPCR and data analysis*

170

171 qPCR was performed with the Sso Advanced Universal SYBR Green Supermix kit (Bio-Rad, 1725271)

172 in an Applied Biosystems StepOnePlus Real-Time PCR Machine (Thermo Fisher Scientific). Commercial

173 primer pairs were used for *GJA1* (Bio-Rad, qHsaCID0012977), as well as *B2M* (Bio-Rad,

174 qHsaCID0015347) and *RPL24* (Bio-Rad, qHsaCID0038677) as housekeeping genes. To prevent gDNA

175 amplification, a DNase digestion step was included during RNA extraction and intron-spanning primer

176 pairs were selected. The amplification program consisted of an initial activation step of 30 s at 95˚C,

177 followed by 50 cycles of 10 s at 95˚C for denaturation and 1 min at 60˚C for annealing and extension, and

178 a final denaturation step of 15 s at 95˚C. Melt curves were performed from 65˚C to 95˚C in steps of 0.5˚C.

179 Technical duplicates of each sample were performed in the qPCR.

180 qPCR data were analyzed with qBase+ software version 3.1 (Biogazelle, Zwijnaarde, Belgium). Only

181 samples with a Ct below 40 were considered for analysis. The expression of each gene was calculated by

182 the $2^{-\Delta\Delta Ct}$ method, normalized to that of undifferentiated hMSCs (assigned value 1) and presented as

183 relative mRNA expression levels.

184

185 *2.7. Neurobiotin (NB) assay*

186

187 A tracer assay was performed to analyze the functionality of GJIC networks. Three replicates of each

188 condition were seeded in chondrogenesis-inducing medium, as described above. After 6 days of

189 differentiation, samples were washed with HBSS buffer without calcium or magnesium (Life

190 Technologies, 14175095) and treated with neurobiotin 2% m v^{-1} (Vector, SP-1120) in HBSS for 90 s at

191 37˚C. Samples were then washed with HBSS, fixed with Formalin Solution, permeabilized with saponin

192 and stained with Streptavidin-Texas Red conjugate (Life Technologies, S872) and Hoechst 1 µg mL^{-1} in

193 BSA 1% m v^{-1} in PBS for 1 h at room temperature. Samples were imaged with a Leica SPE Upright

194 Confocal Microscope as described above.

195 Images were analyzed with ImageJ software. A z-projection of each condensate was created, and

196 background was removed. Distance of neurobiotin spread was measured in a straight line from the outer

197 rim of the condensates' inwards, in at least two separate locations for each condensate.

198

199 *2.8. Condensate transplantation assay*

200

201 Nanopatterns with 18% (S_{18}) and 90% (S_{90}) of local surface adhesiveness were used (Fig. S2 and Table

202 S1). A transplantation assay was performed to study the effects of RGD nanopatterned substrates on

6

203 formed condensates and the propagation of the adhesive information from the substrate into cell
204 condensates. Cells were cultured on the nanopatterns in chondrogenesis-inducing medium as described
205 above. After 3 days, cell condensates formed on the nanopatterns of S_{90} were removed by pipetting and
206 transferred to new S_{90} or S_{18} substrates. Transplanted condensates were cultured on the new substrates for
207 another 3 days, to a total of 6 days of differentiation. For each sample, around half of the condensates
208 were transplanted, whereas the other half were kept on the original substrate (not transplanted) as a
209 control of unaltered differentiation. Three replicates of each condition were seeded and transplanted.
210 Samples were fixed, immunostained, imaged and analyzed for Cx43 expression as described above.
211 Results were normalized to those of non-transplanted S_{90} condensates (assigned value 1) and presented as
212 relative values.
213 To visualize condensates from the side (transversal cuts), Z-stacks were resliced and one image from the
214 center of the condensate was selected. Cx43 production at the basal and top layers of condensates was
215 measured by the average staining intensity at each region on unprocessed images. For each condensate,
216 average basal intensity was divided by average top intensity to obtain the Basal/Top ratio, indicative of
217 Cx43 distribution within condensates.
218
219 *2.9. Integrin blocking and myosin inhibition assays*
220
221 Three replicates of each condition were seeded in chondrogenesis-inducing medium as described above.
222 For integrin blocking samples, medium was changed to fresh medium containing RGD dendrimers in
223 solution at $4 \cdot 10^{-9}\%$ w w^{-1} after 5 days of differentiation. We selected this dendrimer concentration because
224 it yields S_{18} substrates. During substrate functionalization, equilibrium is reached between dendrimer
225 concentration in solution and adsorbed dendrimer density; hence, use of the concentration corresponding
226 to the substrates with the lowest density prevents further adsorption mid-assay.
227 For the myosin inhibition experiment, medium was changed to fresh medium with 50 µg mL^{-1}
228 blebbistatin (Sigma, B0560) 6 h before fixation.
229 All samples were fixed at day 6 of chondrogenesis, immunostained with anti-Cx43 antibody and Sir-
230 Actin (Tebu-bio, SC001), and imaged with a Zeiss LSM780 Confocal Microscope (Zeiss Microscopy)
231 with a 40x objective. Cx43 expression in condensates was quantified as described above and normalized
232 to corresponding non-treated samples.
233
234 *2.10.   Statistics*
235

7

236 Quantitative data are displayed, showing average and standard error of the mean (SEM). n is the sample

237 size. Significant differences were judged using the One-way ANOVA with Fisher LSD post-hoc test or T-

238 test when only two groups are compared, using OriginPro 8.5 or the Simple Interactive Statistical

239 Analysis (SISA) online tool [35]. Where data did not pass a normality test, a Kruskal-Wallis test with

240 Dunn means comparison was applied with GraphPad Prism 8.3. A p of less than 0.05 was considered

241 statistically significant.

242 **3. Results**

243

244 3.1. *Gap junction intercellular communication: Network architecture and functionality*

245

246 We seeded hMSCs on the nanopatterns in chondrogenic medium. Due to the poor interfacing of PLLA

247 with living tissue [36], cells attached preferably through RGD-functionalized dendrimers. Pristine non-

248 patterned PLLA (S_0) and FN-coated (S_{FN}) substrates were the negative and positive controls for cell

249 adhesion, respectively. To control the local surface adhesiveness at the nanoscale during mesenchymal

250 condensation, we used nanopatterns with 18% (S_{18}), 45% (S_{45}) and 90% (S_{90}) of local surface

251 adhesiveness (Fig. S2 and Table S1). Under chondrogenic stimuli, mesenchymal cells aggregate into

252 three-dimensional condensates. While cells on pristine and nanopatterned substrates immediately start

253 aggregating, cells on fibronectin-coated substrates proliferate and adopt a monolayer configuration, from

254 which a few small condensates develop after 3 to 5 days (Fig. S3A) [30]. Condensates in S_{90} maintain

255 their structure in culture up to day 14 (Fig. S3B) [37], while condensates in the rest of the substrates

256 progressively collapse, with detached cells adopting a fibroblast-like morphology (Fig. S3C). We

257 measured the distance between adjacent cell nuclei and found that condensates on high-adherence

258 substrates (S_{90} and S_{FN}) were packed together more tightly than those on low- and mid- adherence ones

259 (Fig. S3D). In the case of large S_{90} condensates, this could be a factor explaining their resistance to

260 collapse through day 14.

261 Intercellular communication through gap junctions is crucial for correct cartilage development. We have

262 previously observed increased expression of chondrogenic markers on S_{90} substrates [30]; we thus

263 wondered if ligand density effects could improve cartilage formation beyond individual cell

264 differentiation. To examine cell-cell interconnectivity through GJ formation, we measured Cx43 in cell

265 condensates. Cx43 is the most widely expressed and studied GJ protein [38] and modulates cartilage

266 structure through its C-terminal cytosolic domain [39]. Connexin hemichannels, or connexons,

267 accumulate and dock with apposed connexons from adjacent cells to form dense GJ plaques. GJIC largely

268 depends on the size of GJ plaques [40] which are continuously regenerated by the addition of connexon

269   subunits at the edges and internalization from the center of the plaques [7,41,42]. Such a continuous

270   renewal may ensure the maintenance of the established GJIC network.

271   We analysed the expression of *GJA1* at day 6 and 9 of chondrogenesis (Fig. 1A). *GJA1* was

272   overexpressed on S_{90} to over twice the level of undifferentiated hMSCs at day 6 and reduced by half on

273   S_{FN}. However, expression on S_{90} levelled off at day 9 among the different nanopattern configurations and

274   S_0. *GJA1* expression in S_{18} and S_{45} nanopatterns is comparable to that of the negative control both at day 6

275   and 9 of chondrogenic induction.

276   Cx43 immunofluorescent images show Cx43 assembled in GJ plaques. Quantification of the percentage

277   of immunostained area showed higher values on S_{90} when compared to most other substrates at day 6 and

278   a slight decrease at day 9, mirroring mRNA expression (Fig. 1B). The fact that Cx43 in GJ plaques on S_{90}

279   is not as high as mRNA expression at day 6 could be explained by a rapid initial turnover [12,41].

280   Confocal z-projections (Fig. 1C, top) of immunostaining show that Cx43 GJ plaques were roughly

281   distributed within the cell condensates with a tendency to accumulate in the outer cell layers, particularly

282   in S_{45}.

283   Skeletonization of Cx43 immunostained images renders a 3D representation of the intercellular

284   communication network (Fig. 1C, bottom, Fig. S1 and Video S1), from which the average branch length

285   (Fig. S4) and number of branch terminations (end-point voxels) can be calculated. Shorter branches and

286   fewer end-point voxels indicate a more intricately shaped GJIC network, as shown in the zoomed-in

287   sections of the skeletonized images of condensates from S_{90} and S_0 nanopatterns. We thus took the

288   number of branch terminations as the inverse index for Cx43 architectural connectivity (Fig. 1D). At days

289   6 and 9 of chondrogenic induction, connectivity progressively increased with local surface adhesiveness

290   up to S_{90} and decreased for S_{FN}.

291   Observation of the spread of biotinylated or fluorescent tracers has become one of the most common

292   methods of demonstrating gap junctions network coupling [43]. Therefore, to further assess GJIC, we

293   conducted a neurobiotin (NB) tracer uptake assay in cell condensates (Fig. 1E). NB is a GJ/hemichannel

294   permeable dye that can penetrate from the exposed Cx43 connexons and diffuse inwards across the GJIC

295   network when Ca^{2+} is maintained below physiological levels (open channel conformation). Quantification

296   of NB diffusion into cell condensates showed NB uptake is significantly higher in S_{90} nanopatterns and

297   equal for all other substrates (Fig. 1F), thereby indicating that S_{90} condensates developed a more efficient

298   GJIC network.
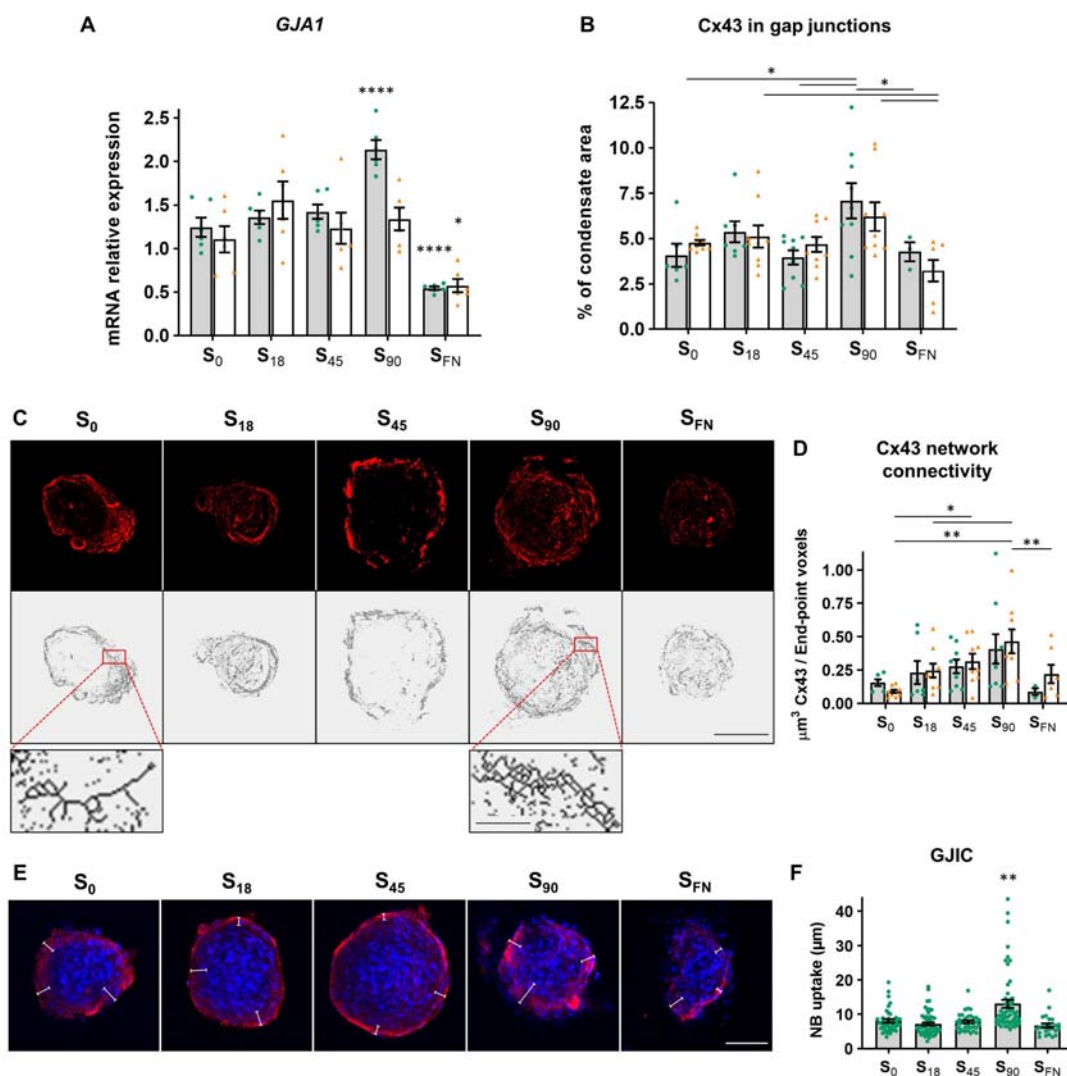
9

Fig. 1: Ligand density modulates gap junction network architecture and function. (**A**) Expression of connexin 43 (*GJA1)* mRNA, relative to that of undifferentiated hMSCs (assigned value 1, not shown) (n=6). (**B**) Percentage of Cx43-stained areas in cell condensates (n≥3). (**C**) Representative confocal z-projections of Cx43 immunostaining (top) and the corresponding skeletonized images (bottom) revealing the branched architecture of the intercellular connectivity network. Scale bar = 40 µm. Zoomed-in sections for the skeletonized images of S_0 and S_{90} highlighting the differences in the GJIC network. Scale bar = 3 µm. (**D**) Quantification of Cx43 architectural network connectivity from skeletonized images normalized against Cx43 in GJs (n≥3). (**E**) Representative confocal z-projections showing neurobiotin (NB) tracer (red) in the mesenchymal condensates and cell nuclei stained with Hoechst (blue). White lines represent measured distances of neurobiotin uptake. Scale bar = 80 µm. (**F**) Quantification of neurobiotin tracer uptake in day 6 condensates after 90 s exposure (n≥24). Gray bars with green dots correspond to day 6 of chondrogenic induction; white bars with orange triangles correspond to day 9. Results are given as individual sample values with the mean ± SEM, **p<0.05*, ***p<0.01*, ****p<0.0001*

10

312   *3.2. Matrix adhesion continually regulates GJIC*

313

314   Results showed an effect of local surface adhesiveness on the architecture and functionality of GJIC

315   networks in pre-cartilaginous cell condensates. However, it was unclear whether substrate adhesion is

316   relevant only at the beginning of condensation as a memory effect or if it continuously influences the

317   tissue as it forms. To consider these two possibilities, we designed a transplantation assay in which

318   condensates formed on S_{90} and $S_{18,}$ (the nanopatterns of highest and lowest ligand density) were collected

319   at day 3, plated on new S_{90} and S_{18} substrates and maintained for 3 more days in culture (Fig. 2A). The

320   percentage of area immunostained for Cx43 (GJ plaques) was assessed at day 6 for the transplanted and

321   non-transplanted condensates. Transplantation produced a significant boosting effect for condensates

322   plated on new S_{90} substrates (Fig. 2B). In condensates transplanted from S_{90} to fresh S_{90}, Cx43 production

323   increased by $71\pm21\%$, while a $61\pm19\%$ increase was observed for those transplanted from S_{18}.

324   Transplantation of either S_{90} or S_{18} condensates to fresh S_{18} substrates did not render significant changes

325   in Cx43 production.

326   Condensates formed on one substrate and then transplanted to another will sense the new input only from

327   the side in direct contact with the new substrate. We questioned if effects derived from changing substrate

328   conditions would be confined to cells in direct contact with it (those at the basal layer of condensates) or

329   instead propagate to the middle and top layers of condensates. Transversal views of transplanted

330   condensates presented increased Cx43 production at all heights (Fig. 2C), showing that fresh substrate

331   inputs spread through cells and modulate protein expression within the whole forming tissue. Moreover,

332   the proportion of Cx43 production between the basal versus top regions was equal in control and

333   transplanted condensates, indicating that transplantation did not alter the ratios of protein distribution

334   among layers (Fig. 2D).

11
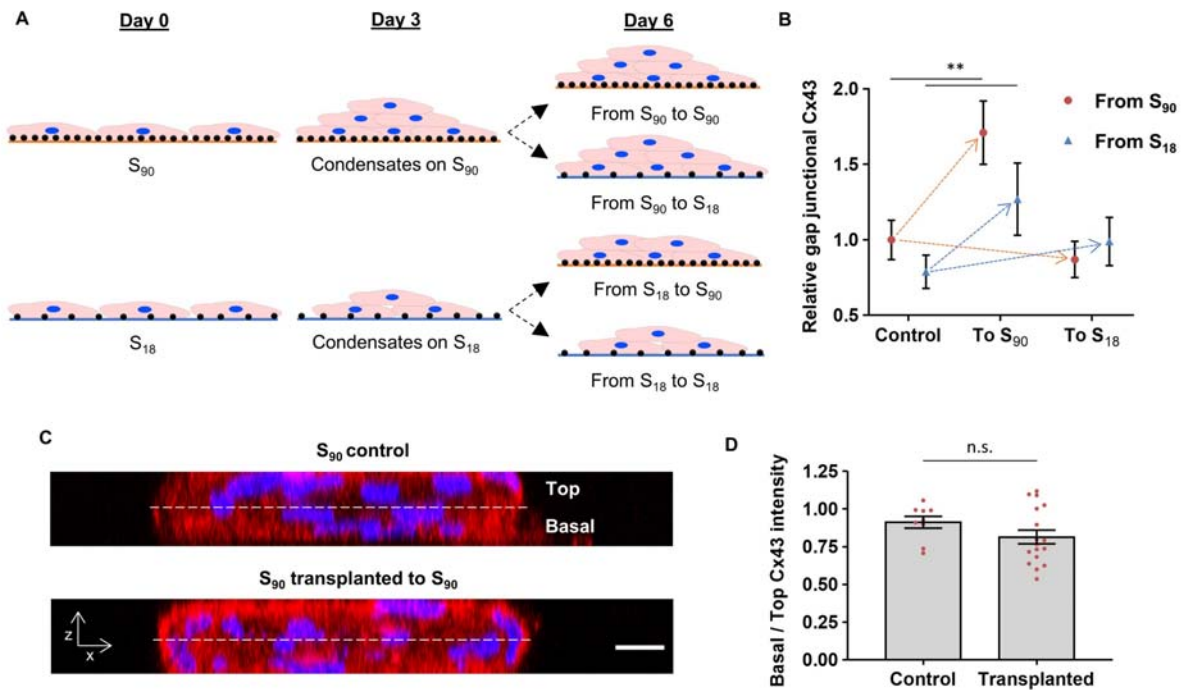
Fig. 2: Cell condensates adapt to changing ligand density. (A) Schematics of the transplantation experiment. Condensates formed on S_{90} and S_{18} substrates were collected at day 3 and plated on fresh S_{90} or S_{18} substrates for 3 more days of chondrogenic induction. **(B)** Quantification of Cx43-stained percentage area for non-transplanted and transplanted condensates ($n \geq 7$). **(C)** Confocal side views of control and transplanted S_{90} condensates, stained for Cx43 (red) and Hoechst (blue). Substrate effect propagates to cells at all levels within condensates. Scale bar = 10 μm. **(D)** Ratio between Cx43 production at the basal and top regions of S_{90} condensates in control S_{90} substrates or transplanted to fresh S_{90} ($n \geq 9$). Results are given as mean ± SEM, **$p < 0.01$

343 *3.3. Mechanism of substrate sensing and input propagation*

344

345 Integrin adhesions are the main mediators of cell-matrix adhesion and mechanical interactions [44,45]. To

346 evaluate their role in modulating GJIC on nanopatterns, we added RGD-functionalized dendrimers in

347 solution on formed condensates to block integrin receptors at the cell membrane. Disturbance of integrin

348 clustering at cell-substrate adhesion sites led to a Cx43 production decrease in S_{90} but not in S_{18} (Fig. 3A).

349 This indicates that integrin-mediated cell adhesion is responsible for the transduction and regulation of

350 substrate information that affects GJIC, and that cell response is triggered when integrins are engaged by

351 the RGD configuration provided by S_{90} nanopatterns.

352 Since perturbations at the cell membrane are transduced into chemical responses by propagation from

353 integrins through the cytoskeleton [16], we hypothesized that the substrate adhesion information

354 orchestrating GJIC during mesenchymal cell condensation propagates through the actin cortex. Cortical

355 actin assembly can be observed in early mesenchymal condensates [30]. Cortical tension gradients are

356 responsible for mesenchymal cell rearrangement during tissue formation and are essential in driving

357 tissue morphogenesis [46,47]. The cell cortex is formed by an actomyosin network, which is located

358 below the cell membrane. In the cortex, myosin-2 pulls on actin filaments and generates tension.

359 Inhibition of myosin-2 activity can cause a decrease in cortical tension of up to 80% [47]. Treatment of 6-

360 day condensates with the myosin-2 inhibitor blebbistatin decreased the percentage of area immunostained

361 for Cx43 of S_{90} condensates (Fig. 3A).

362 Adding dendrimers in solution affected cytoskeletal conformation in a similar manner as blebbistatin,

363 preventing polymerization and resulting in a diffuse distribution of actin in condensates, instead of

364 concentrating in clearly defined fibers as in control conditions (Fig. 3B). This shows that cytoskeletal

365 tension depends on integrin receptors engaging adherence sites at the substrates; we thus infer that cells at

366 the basal layer of condensates sense ligand inputs through integrins and propagate them by actin

367 contractility to adjacent cells (Fig. 3C).

13

368
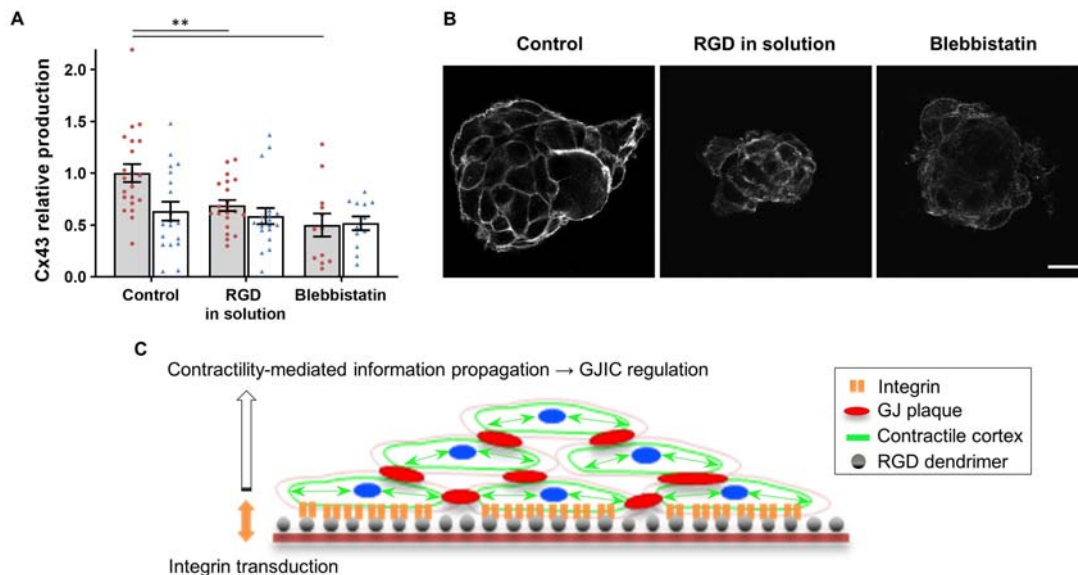
Fig. 3: Signal transduction and propagation. (A) Relative Cx43 production in S_{90} (gray bars, red dots) and S_{18} (white bars, blue triangles) (n≥12). Results are given as mean ± SEM, **p<0.01. **(B)** Actin staining for S_{90} condensates at day 6 in control conditions, with RGD dendrimers in solution (integrin block) or with blebbistatin (myosin inhibition). Scale bar = 25 µm. **(C)** Schematic representation of ligand density sensing through integrin adhesions, followed by actomyosin contraction-guided propagation of information in cell condensates.

4. Discussion

We studied the effects of ECM adhesion in the establishment of GJIC during mesenchymal cell condensation, a prevalent morphogenetic transition. To this end, we used previously developed RGD dendrimer-based nanopatterns of tunable local surface adhesiveness [29,30]. Larger and more stable cell condensates are obtained on S_{90} nanopatterns, with cells packed closer together.

We analyzed the influence of substrate ligand density on the establishment of a gap junction intercellular communication (GJIC) network in cell condensates. We measured gene expression and assembly at gap junctions of Cx43, a connexin which is ubiquitously expressed in developing cartilage [39,48]. We found Cx43 increased with local surface adhesiveness in the nanopatterns, a similar interdependence to what we observed previously for the focal adhesion adaptor protein paxillin [30]. This is in agreement with Zhou *et al*., who observed a direct interaction between FAK and paxillin with Cx43 in cells from the human apical papilla, which depended on substrate compliance [13]. In our case, cell condensates on S_{90} nanopatterns

14

389   presented increased Cx43 expression with a higher protein turnover rate, revealing a direct effect of

390   substrate ligand density on gap junction protein regulation.

391   We analyzed the architectural connectivity of Cx43 in condensates to assess whether substrate ligand

392   density modulates the development of gap junction networks beyond protein expression. We found that

393   S_{90} condensates contain a Cx43 architecture that is more intricate, with less end-point voxels and shorter

394   branches, indicative of improved communication capacities. Moreover, a tracer uptake assay revealed that

395   GJIC is more efficient on S_{90} condensates. This shows that local surface adhesiveness given by the

396   nanopattern configuration determines not only protein expression but also its spatial disposition during

397   morphogenesis, affecting the functionality of the forming tissue. Given that S_{90} substrates also promote

398   cell differentiation towards chondrocytes [30], we conclude that nanopatterning at this particular ligand

399   density improves cartilage formation *in vitro*.

400   A condensate transplantation assay was designed to test whether cells in the condensate, previously in

401   contact with the substrate during cell recruitment, retain initial substrate information (memory effect) or

402   receive a continuous feedback of substrate input. Transplantation of cell condensates to a new S_{90}

403   substrate caused a significant increase in Cx43, suggesting that cell condensates still preserve a certain

404   level of mesenchymal plasticity at early stages of chondrogenic differentiation [49], thereby allowing

405   phenotype reconfiguration in response to the ECM input. No effects were observed for transplantation to

406   S_{18} substrates.

407   Effects of substrate transplantation on Cx43 expression were observed at all heights within condensates

408   and transplanted condensates maintained the proportion of total protein contained at the basal and top

409   regions, indicating that substrate inputs are propagated into the third dimension, across cells to the top.

410   These results show that changing environmental conditions during morphogenesis continually modulate

411   the characteristics of forming tissue, pointing to the importance of accounting for time variations in the

412   design of experimental setups for development studies, as well as biomaterials for tissue engineering.

413   Finally, we addressed the biological mechanism by which cells sense substrate ligand density and

414   propagate it into condensates. Blocking integrin-mediated interactions between the substrate and the basal

415   layer in cell condensates caused a Cx43 decrease in S_{90} but not in S_{18}. This observation, together with

416   results of condensate stability and GJIC, demonstrates that the establishment of GJIC during

417   mesenchymal condensation is an adhesion-gated mechanism, in which S_{90} nanopattern configuration

418   provides optimal ligand density and distribution to trigger cell response.

419   To investigate the propagation of substrate information within cell condensates, an inhibition experiment

420   for myosin-2 was conducted. Inhibition of myosin-2 activity by blebbistatin caused a decrease of Cx43 in

421   S_{90} cell condensates, in agreement with previous reports [50]. This indicates that once integrins are

422   engaged, the adhesion information from the substrate is transduced and propagates through the actin

15

423   filaments by myosin-2 mediated contraction, which in turn can regulate GJ accretion through ZO-1[12].

424   Results agree with those from Gowrishankar *et al*., who predicted that the dynamics of membrane

425   proteins are regulated by the cell cortex [51]. Therefore, we propose a contractility-based mechanism for

426   the propagation of ECM adhesion information within the condensates in which local substrate

427   adhesiveness induces a rearrangement and adaptation of the actin cortex and cell-cell junctions in the first

428   cell layers [52,53] and propagates through the tissue by myosin-2-mediated cortex contractions, regulating

429   Cx43 dynamics during the mesenchymal condensation process (Fig. 3C).

430   Our findings clearly reflect the impact that the fine tuning of materials interfaces has in cell response. By

431   tailoring the nanopattern configuration of the cell-adhesive motif RGD, we exerted control over the

432   architecture and function of a complex dynamic biological system. The results have an immediate

433   application to cartilage *in vitro* engineering [30,54], but they are also extensible to the study of other

434   biological processes in which active ECM remodelling and thus, changes in the adhesion requirements

435   and intercellular communication play an active role, such as in cancer progression [55].

436

CRediT author statement

438   **I. Casanellas:** Conceptualization, Methodology, Investigation, Formal analysis, Writing – Original Draft,

439   Visualization. **A. Lagunas:** Conceptualization, Methodology, Formal analysis, Writing – Original Draft,

440   Supervision, Project administration, Funding acquisition. **Y. Vida:** Methodology, Resources (design and

441   production of RGD-functionalized dendrimers), Writing – Review & Editing. **E. Pérez-Inestrosa**:

442   Methodology, Resources (design and production of RGD-functionalized dendrimers), Writing – Review

443   & Editing, Funding acquisition. **C. Rodríguez-Pereira:** Methodology, Investigation, Formal analysis

444   (RT-qPCR), Writing – Review & Editing. **J. Magalhaes:** Methodology (RT-qPCR), Supervision, Writing

445   – Review & Editing. **J. A. Andrades:** Writing – Review & Editing, Funding acquisition. **J. Becerra:**

446   Writing – Review & Editing, Funding acquisition. **J. Samitier:** Conceptualization, Methodology, Writing

447   – Review & Editing, Supervision, Project administration, Funding acquisition.

448

468

Conflicts of interest

470   There are no conflicts to declare.

471

475

References

477

478   [1]   A.M. DeLise, L. Fischer, R.S. Tuan, Cellular interactions and signaling in cartilage development,

479   Osteoarthr. Cartil. 8 (2000) 309–334. https://doi.org/10.1053/joca.1999.0306.

480   [2]   H. Grüneberg, The pathology of development: a study of inherited skeletal disorders in animals,

481   Blackwells Scientific Publications, Oxford, 1963.

482   [3]   S. Christley, M.S. Alber, S.A. Newman, Patterns of mesenchymal condensation in a multiscale,

483   discrete stochastic model, PLoS Comput. Biol. 3 (2007) 743–753.

484   https://doi.org/10.1371/journal.pcbi.0030076.

485   [4]   P. Singh, J.E. Schwarzbauer, Fibronectin and stem cell differentiation - lessons from

486   chondrogenesis, J. Cell Sci. 125 (2012) 3703–3712. https://doi.org/10.1242/jcs.095786.

487   [5]   C.N.D. Coelho, R.A. Kosher, Gap junctional communication during limb cartilage differentiation,

488   Dev. Biol. 144 (1991) 47–53. https://doi.org/https://doi.org/10.1016/0012-1606(91)90477-K.

489   [6]   J.C. Hervé, M. Derangeon, Gap-junction-mediated cell-to-cell communication, Cell Tissue Res.
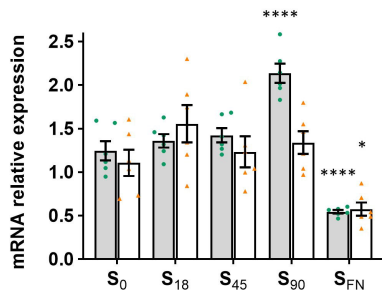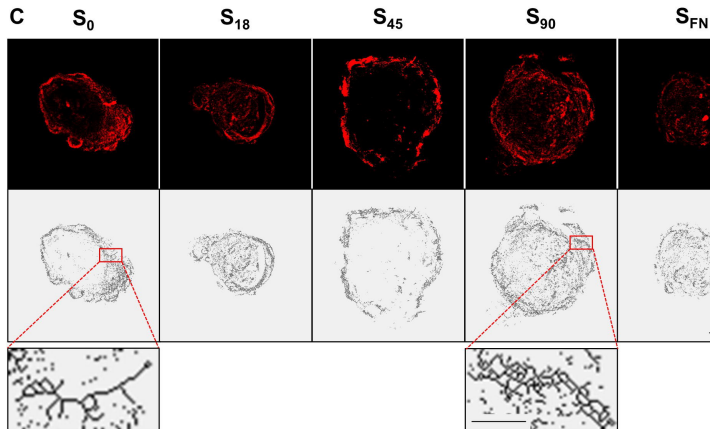
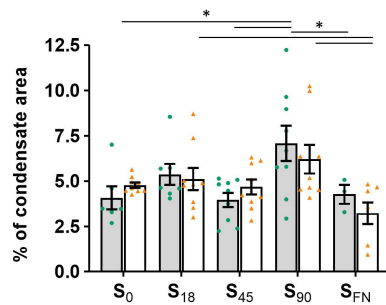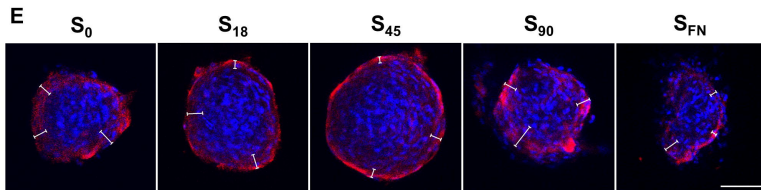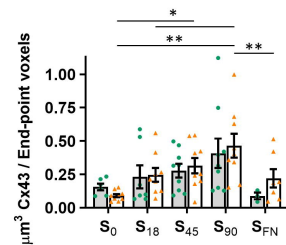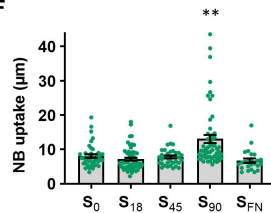490   352 (2013) 21–31. https://doi.org/10.1007/s00441-012-1485-6.

491 [7] J.C. Hervé, M. Derangeon, D. Sarrouilhe, B.N.G. Giepmans, N. Bourmeyster, Gap junctional
492   channels are parts of multiprotein complexes, Biochim. Biophys. Acta - Biomembr. 1818 (2012)
493   1844–1865. https://doi.org/10.1016/j.bbamem.2011.12.009.

494 [8] M.D. Mayan, R. Gago-Fuentes, P. Carpintero-Fernandez, P. Fernandez-Puente, P. Filgueira-
495   Fernandez, N. Goyanes, V. Valiunas, P.R. Brink, G.S. Goldberg, F.J. Blanco, Articular
496   chondrocyte network mediated by gap junctions: Role in metabolic cartilage homeostasis, Ann.
497   Rheum. Dis. 74 (2015) 275–284. https://doi.org/10.1136/annrheumdis-2013-204244.

498 [9] H.J. Donahue, R.W. Qu, D.C. Genetos, Joint diseases: From connexins to gap junctions, Nat. Rev.
499   Rheumatol. 14 (2018) 42–51. https://doi.org/10.1038/nrrheum.2017.204.

500 [10] P.D. Lampe, B.P. Nguyen, S. Gil, M. Usui, J. Olerud, W.G. Carter, Y. Takada, Cellular interaction
501   of integrin α3β1 with laminin 5 promotes gap junctional communication, J. Cell Biol. 143 (1998)
502   1735–1747. https://doi.org/10.1083/jcb.143.6.1735.

503 [11] N. Batra, S. Burra, A.J. Siller-Jackson, S. Gu, X. Xia, G.F. Weber, D. DeSimone, L.F. Bonewald,
504   E.M. Lafer, E. Sprague, M.A. Schwartz, J.X. Jiang, Mechanical stress-activated integrin α5β1
505   induces opening of connexin 43 hemichannels, Proc. Natl. Acad. Sci. 109 (2012) 3359–3364.
506   https://doi.org/10.1073/pnas.1115967109.

507 [12] A.E. Zemljic-Harpf, J.C. Godoy, O. Platoshyn, E.K. Asfaw, A.R. Busija, A.A. Domenighetti, R.S.
508   Ross, Vinculin directly binds zonula occludens-1 and is essential for stabilizing connexin-43-
509   containing gap junctions in cardiac myocytes, J. Cell Sci. 127 (2014) 1104–1116.
510   https://doi.org/10.1242/jcs.143743.

511 [13] C. Zhou, D. Zhang, W. Du, J. Zou, X. Li, J. Xie, Substrate mechanics dictate cell-cell
512   communication by gap junctions in stem cells from human apical papilla, Acta Biomater. 107
513   (2020) 178–193. https://doi.org/10.1016/j.actbio.2020.02.032.

514 [14] B.M. Gumbiner, Cell adhesion: The molecular basis of tissue architecture and morphogenesis,
515   Cell. 84 (1996) 345–357. https://doi.org/10.1016/S0092-8674(00)81279-9.

516 [15] J.T. Parsons, A.R. Horwitz, M.A. Schwartz, Cell adhesion: Integrating cytoskeletal dynamics and
517   cellular tension, Nat. Rev. Mol. Cell Biol. 11 (2010) 633–643. https://doi.org/10.1038/nrm2957.

518 [16] M. Bachmann, S. Kukkurainen, V.P. Hytönen, B. Wehrle-Haller, Cell adhesion by integrins,
519   Physiol. Rev. 99 (2019) 1655–1699. https://doi.org/10.1152/physrev.00036.2018.

520 [17] D.C. Van Essen, A tension-based theory of morphogenesis and compact wiring in the central
521   nervous system, Nature. 385 (1997) 313–318. https://doi.org/10.1038/385313a0.

522 [18] M. Tada, M.L. Concha, Vertebrate gastrulation: Calcium waves orchestrate cell movements, Curr.
523   Biol. 11 (2001) 470–472. https://doi.org/10.1016/S0960-9822(01)00284-6.

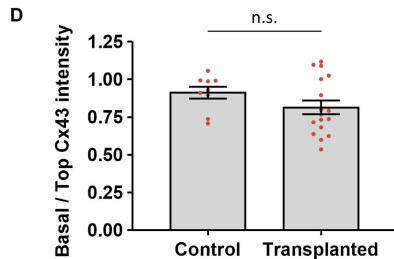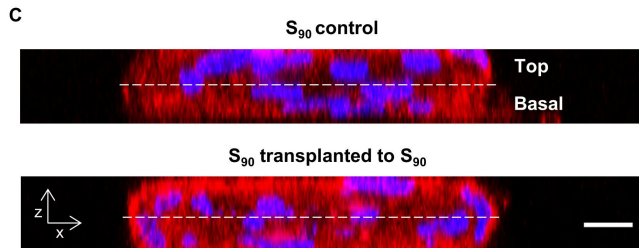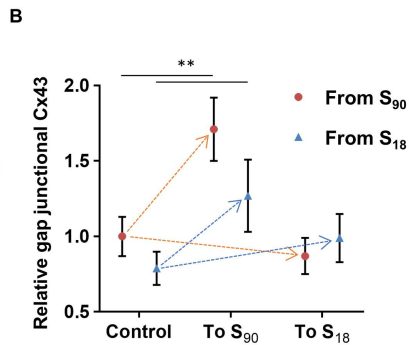524 [19] Hung Ping Shih, D. Panlasigui, V. Cirulli, M. Sander, ECM signaling regulates collective cellular
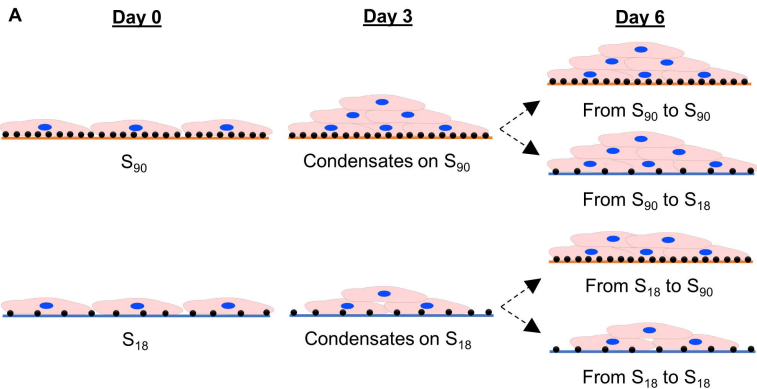
525   dynamics to control pancreas branching morphogenesis, Cell Rep. 14 (2016) 169–179.

526   https://doi.org/10.1016/j.celrep.2015.12.027.

527   [20]   F. Jiang, H. Hörber, J. Howard, D.J. Müller, Assembly of collagen into microribbons: Effects of

528   pH and electrolytes, J. Struct. Biol. 148 (2004) 268–278. https://doi.org/10.1016/j.jsb.2004.07.001.

529   [21]   M.L. Smith, D. Gourdon, W.C. Little, K.E. Kubow, R.A. Eguiluz, S. Luna-Morris, V. Vogel,

530   Force-induced unfolding of fibronectin in the extracellular matrix of living cells, PLoS Biol. 5

531   (2007) 2243–2254. https://doi.org/10.1371/journal.pbio.0050268.

532   [22]   W.C. Little, M.L. Smith, U. Ebneter, V. Vogel, Assay to mechanically tune and optically probe

533   fibrillar fibronectin conformations from fully relaxed to breakage, Matrix Biol. 27 (2008) 451–

534   461. https://doi.org/10.1016/j.matbio.2008.02.003.

535   [23]   M.F. Garcia-Parajo, A. Cambi, J.A. Torreno-Pina, N. Thompson, K. Jacobson, Nanoclustering as a

536   dominant feature of plasma membrane organization, J. Cell Sci. 127 (2014) 4995–5005.

537   https://doi.org/10.1242/jcs.146340.

538   [24]   M. Arnold, E.A. Cavalcanti-Adam, R. Glass, J. Blümmel, W. Eck, M. Kantlehner, H. Kessler, J.P.

539   Spatz, Activation of integrin function by nanopatterned adhesive interfaces, ChemPhysChem. 5

540   (2004) 383–388. https://doi.org/10.1002/cphc.200301014.

541   [25]   E.A. Cavalcanti-Adam, T. Volberg, A. Micoulet, H. Kessler, B. Geiger, J.P. Spatz, Cell spreading

542   and focal adhesion dynamics are regulated by spacing of integrin ligands, Biophys. J. 92 (2007)

543   2964–2974. https://doi.org/10.1529/biophysj.106.089730.

544   [26]   J.A. Deeg, I. Louban, D. Aydin, C. Selhuber-Unkel, H. Kessler, J.P. Spatz, Impact of local versus

545   global ligand density on cellular adhesion, Nano Lett. 11 (2011) 1469–1476.

546   https://doi.org/10.1021/nl104079r.

547   [27]   R. Oria, T. Wiegand, J. Escribano, A. Elosegui-Artola, J.J. Uriarte, C. Moreno-Pulido, I. Platzman,

548   P. Delcanale, L. Albertazzi, D. Navajas, X. Trepat, J.M. García-Aznar, E.A. Cavalcanti-Adam, P.

549   Roca-Cusachs, Force loading explains spatial sensing of ligands by cells, Nature. 552 (2017) 219–

550   224. https://doi.org/10.1038/nature24662.

551   [28]   A. Lagunas, D. Caballero, J. Samitier, Influence of Controlled Micro☐ and Nanoengineered

552   Environments on Stem Cell Fate, in: A. Tiwari, B. Garipcan, L. Uzun (Eds.), Adv. Surfaces Stem

553   Cell Res., 1st ed., Hoboken: Wiley, 2016: pp. 87–141.

554   [29]   A. Lagunas, A.G. Castaño, J.M. Artés, Y. Vida, D. Collado, E. Pérez-Inestrosa, P. Gorostiza, S.

555   Claros, J.A. Andrades, J. Samitier, Large-scale dendrimer-based uneven nanopatterns for the study

556   of local arginine-glycine-aspartic acid (RGD) density effects on cell adhesion, Nano Res. 7 (2014)

557   399–409. https://doi.org/10.1007/s12274-014-0406-2.

558   [30]   A. Lagunas, I. Tsintzou, Y. Vida, D. Collado, E. Pérez-Inestrosa, C. Rodríguez Pereira, J.

19

559   Magalhaes, J.A. Andrades, J. Samitier, Tailoring RGD local surface density at the nanoscale

560   toward adult stem cell chondrogenic commitment, Nano Res. 10 (2017) 1959–1971.

561   https://doi.org/10.1007/s12274-016-1382-5.

562   [31]   I. Casanellas, A. Lagunas, I. Tsintzou, Y. Vida, D. Collado, E. Pérez-Inestrosa, C. Rodríguez-

563   Pereira, J. Magalhaes, P. Gorostiza, J.A. Andrades, J. Becerra, J. Samitier, Dendrimer-based

564   uneven nanopatterns to locally control surface adhesiveness: A method to direct chondrogenic

565   differentiation, J. Vis. Exp. 131 (2018). https://doi.org/10.3791/56347.

566   [32]   I. Casanellas, A. Lagunas, Y. Vida, E. Pérez-Inestrosa, J.A. Andrades, J. Becerra, J. Samitier,

567   Matrix nanopatterning regulates mesenchymal differentiation through focal adhesion size and

568   distribution according to cell fate, Biomimetics. 4 (2019).

569   https://doi.org/10.3390/biomimetics4020043.

570   [33]   B.E. Bobick, F.H. Chen, A.M. Le, R.S. Tuan, Regulation of the chondrogenic phenotype in

571   culture, Birth Defects Res. Part C - Embryo Today Rev. 87 (2009) 351–371.

572   https://doi.org/10.1002/bdrc.20167.

573   [34]   I. Horcas, R. Fernández, J.M. Gómez-Rodríguez, J. Colchero, J. Gómez-Herrero, A.M. Baro,

574   WSXM: A software for scanning probe microscopy and a tool for nanotechnology, Rev. Sci.

575   Instrum. 78 (2007). https://doi.org/10.1063/1.2432410.

576   [35]   D.G. Uitenbroek, SISA Binomial, (1997). http://www.quantitativeskills.com/sisa/statistics/t-

577   test.htm (accessed January 30, 2020).

578   [36]   Y. Zhu, C. Gao, X. Liu, T. He, J. Shen, Immobilization of Biomacromolecules onto Aminolyzed

579   Poly(L-lactic acid) toward Acceleration of Endothelium Regeneration, Tissue Eng. 10 (2004) 53–

580   61. https://doi.org/10.1089/107632704322791691.

581   [37]   I. Casanellas, A. Lagunas, Y. Vida, P. Ezequiel, J.A. Andrades, J. Becerra, J. Samitier, The Janus

582   role of adhesion in chondrogenesis, Int. J. Mol. Sci. 21 (2020) 5269.

583   https://doi.org/10.3390/ijms21155269.

584   [38]   T.M. Ribeiro-Rodrigues, T. Martins-Marques, S. Morel, B.R. Kwak, H. Girão, Role of connexin

585   43 in different forms of intercellular communication - gap junctions, extracellular vesicles and

586   tunnelling nanotubes, J. Cell Sci. 130 (2017) 3619–3630. https://doi.org/10.1242/jcs.200667.

587   [39]   R. Gago-Fuentes, J.F. Bechberger, M. Varela-Eirin, A. Varela-Vazquez, B. Acea, E. Fonseca, C.C.

588   Naus, M.D. Mayan, The C-terminal domain of connexin43 modulates cartilage structure via

589   chondrocyte phenotypic changes, Oncotarget. 7 (2016) 73055–73067.

590   https://doi.org/10.18632/oncotarget.12197.

591   [40]   J.M. Rhett, J. Jourdan, R.G. Gourdie, Connexin 43 connexon to gap junction transition is regulated

592   by zonula occludens-1, Mol. Biol. Cell. 22 (2011) 1516–1528. https://doi.org/10.1091/mbc.E10-
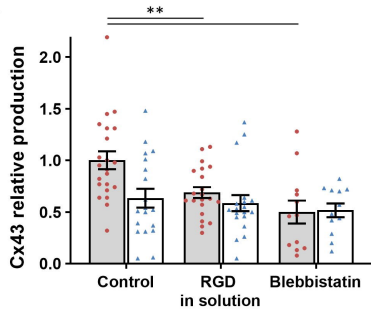
593   06-0548.

594   [41]   E. Leithe, S. Sirnes, T. Fykerud, A. Kjenseth, E. Rivedal, Endocytosis and post-endocytic sorting
595   of connexins, Biochim. Biophys. Acta - Biomembr. 1818 (2012) 1870–1879.
596   https://doi.org/10.1016/j.bbamem.2011.09.029.

597   [42]   M. Piehl, C. Lehmann, A. Gumpert, J.-P. Denizot, D. Segretain, M.M. Falk, Internalization of
598   Large Double-Membrane Intercellular Vesicles by a Clathrin-dependent Endocytic Process, Mol.
599   Biol. Cell. 18 (2007) 337–347. https://doi.org/10.1091/mbc.E06.

600   [43]   J. Jacoby, A. Nath, Z.F. Jessen, G.W. Schwartz, A Self-Regulating Gap Junction Network of
601   Amacrine Cells Controls Nitric Oxide Release in the Retina, Neuron. 100 (2018) 1149-1162.e5.
602   https://doi.org/10.1016/j.neuron.2018.09.047.

603   [44]   Z. Sun, S.S. Guo, R. Fässler, Integrin-mediated mechanotransduction, J. Cell Biol. 215 (2016)
604   445–456.

605   [45]   J.Z. Kechagia, J. Ivaska, P. Roca-Cusachs, Integrins as biomechanical sensors of the
606   microenvironment, Nat. Rev. Mol. Cell Biol. (2019). https://doi.org/10.1038/s41580-019-0134-2.

607   [46]   M. Nishikawa, S.R. Naganathan, F. Jülicher, S.W. Grill, Controlling contractile instabilities in the
608   actomyosin cortex, Elife. 6 (2017) 1–21. https://doi.org/10.7554/eLife.19595.

609   [47]   H. Tao, M. Zhu, K. Lau, O.K.W. Whitley, M. Samani, X. Xiao, X.X. Chen, N.A. Hahn, W. Liu,
610   M. Valencia, M. Wu, X. Wang, K.D. Fenelon, C.C. Pasiliao, D. Hu, J. Wu, S. Spring, J. Ferguson,
611   E.P. Karuna, R.M. Henkelman, A. Dunn, H. Huang, H.Y.H. Ho, R. Atit, S. Goyal, Y. Sun, S.
612   Hopyan, Oscillatory cortical forces promote three dimensional cell intercalations that shape the
613   murine mandibular arch, Nat. Commun. 10 (2019) 1–18. https://doi.org/10.1038/s41467-019-
614   09540-z.

615   [48]   R.A. Meyer, M.F. Cohen, S. Recalde, J. Zakany, S.M. Bell, W.J.J. Scott, C.W. Lo, Developmental
616   regulation and asymmetric expression of the gene encoding Cx43 gap junctions in the mouse limb
617   bud., Dev. Genet. 21 (1997) 290–300. https://doi.org/10.1002/(SICI)1520-
618   6408(1997)21:4<290::AID-DVG6>3.0.CO;2-2.

619   [49]   Y. Liu, N. Muñoz, A.C. Tsai, T.M. Logan, T. Ma, Metabolic Reconfiguration Supports
620   Reacquisition of Primitive Phenotype in Human Mesenchymal Stem Cell Aggregates, Stem Cells.
621   35 (2017) 398–410. https://doi.org/10.1002/stem.2510.

622   [50]   S. Olk, G. Zoidl, R. Dermietzel, Connexins, cell motility, and the cytoskeleton, Cell Motil.
623   Cytoskeleton. 66 (2009) 1000–1016. https://doi.org/10.1002/cm.20404.

624   [51]   K. Gowrishankar, S. Ghosh, S. Saha, C. Rumamol, S. Mayor, M. Rao, Active remodeling of
625   cortical actin regulates spatiotemporal organization of cell surface molecules, Cell. 149 (2012)
626   1353–1367. https://doi.org/10.1016/j.cell.2012.05.008.

627   [52]   N. Wang, J.D. Tytell, D.E. Ingber, Mechanotransduction at a distance: Mechanically coupling the

628   extracellular matrix with the nucleus, Nat. Rev. Mol. Cell Biol. 10 (2009) 75–82.

629   https://doi.org/10.1038/nrm2594.

630   [53]   P. Chugh, E.K. Paluch, The actin cortex at a glance, J. Cell Sci. 131 (2018) 1–9.

631   https://doi.org/10.1242/jcs.186254.

632   [54]   C. Rodríguez-Pereira, A. Lagunas, I. Casanellas, Y. Vida, E. Pérez-Inestrosa, J.A. Andrades, J.

633   Becerra, J. Samitier, F.J. Blanco, J. Magalhães, RGD-dendrimer-poly(L-lactic) acid nanopatterned

634   substrates for the early chondrogenesis of human mesenchymal stromal cells derived from

635   osteoarthritic and healthy donors, Materials (Basel). 13 (2020).

636   https://doi.org/10.3390/ma13102247.

637   [55]   C. Bonnans, J. Chou, Z. Werb, Remodelling the extracellular matrix in development and disease,

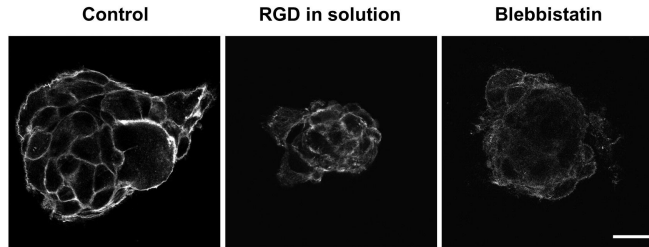638   Nat. Rev. Mol. Cell Biol. 15 (2014) 786–801. https://doi.org/10.1038/nrm3904.

639

A *GJA1*

B Cx43 in gap junctions

C

D Cx43 network connectivity

E

F GJIC

A Day 0 Day 3 Day 6

S_{90}

Condensates on S_{90}

From S_{90} to S_{90}

From S_{90} to S_{18}

S_{18}

Condensates on S_{18}

From S_{18} to S_{90}

From S_{18} to S_{18}

B

Relative gap junctional Cx43

Control   To S_{90} To S_{18}

From S_{90}
From S_{18}

**

C

S_{90} control

Top
Basal

S_{90} transplanted to S_{90}

z
x

D

Basal / Top Cx43 intensity

Control   Transplanted

n.s.

A

Cx43 relative production

B Control | RGD in solution | Blebbistatin

C

Contractility-mediated information propagation → GJIC regulation

Integrin transduction

Legend:
- Integrin
- GJ plaque
- Contractile cortex
- RGD dendrimer